

# The imprint of carbon combustion on a superburst from the accreting neutron star 4U 1636–536

L. Keek,<sup>1\*</sup> A. Cumming,<sup>2</sup> Z. Wolf,<sup>1</sup> D.R. Ballantyne,<sup>1</sup> V.F. Suleimanov,<sup>3,4</sup>  
E. Kuulkers,<sup>5</sup> T.E. Strohmayer<sup>6</sup>

<sup>1</sup>Center for Relativistic Astrophysics, School of Physics, Georgia Institute of Technology, 837 State Street, Atlanta, GA 30332-0430, USA

<sup>2</sup>Department of Physics, McGill University, 3600 rue University, Montreal, QC, H3A 2T8, Canada

<sup>3</sup>Institut für Astronomie und Astrophysik, Kepler Center for Astro and Particle Physics, Universität Tübingen, Sand 1, 72076 Tübingen, Germany

<sup>4</sup>Kazan (Volga region) Federal University, Kremlevskaja str., 18, Kazan 420008, Russia

<sup>5</sup>European Space Astronomy Centre (ESA/ESAC), Science Operations Department, 28691 Villanueva de la Cañada, Madrid, Spain

<sup>6</sup>X-ray Astrophysics Lab, Astrophysics Science Division, NASA's Goddard Space Flight Center, Greenbelt, MD 20771, USA

Accepted XXX. Received YYY; in original form ZZZ

## ABSTRACT

Superbursts are hours-long X-ray flares attributed to the thermonuclear runaway burning of carbon-rich material in the envelope of accreting neutron stars. By studying the details of the X-ray light curve, properties of carbon combustion can be determined. In particular, we show that the shape of the rise of the light curve is set by the the slope of the temperature profile left behind by the carbon flame. We analyse *RXTE*/PCA observations of 4U 1636–536 and separate the direct neutron star emission from evolving photoionized reflection and persistent spectral components. This procedure results in the highest quality light curve ever produced for the superburst rise and peak, and interesting behaviour is found in the tail. The rising light curve between 100 and 1000 seconds is inconsistent with the idea that the fuel burned locally and instantaneously everywhere, as assumed in some previous models. By fitting improved cooling models, we measure for the first time the radial temperature profile of the superbursting layer. We find  $d \ln T / d \ln P \approx 1/4$ . Furthermore, 20 % of the fuel may be left unburned. This gives a new constraint on models of carbon burning and propagation in superbursts.

**Key words:** accretion, accretion disks — stars: neutron — stars: individual: 4U 1636-536 — X-rays: binaries — X-rays: bursts

## 1 INTRODUCTION

In the past decade rare long (hours–day) X-ray flares have been observed from neutron stars that accrete from a companion star in low-mass X-ray binaries (Cornelisse et al. 2000). In contrast to the shorter (10–100 s) Type I X-ray bursts powered by hydrogen/helium flashes (e.g., Lewin et al. 1993), these so-called superbursts are thought to arise from runaway carbon fusion in the ashes of hydrogen and helium burning (Strohmayer & Brown 2002; Cumming & Bildsten 2001).

Cumming & Macbeth (2004) assumed that after superburst ignition the carbon would rapidly undergo complete burning to iron group elements, and modelled the superburst light curve by numerically following the subsequent cooling of the neutron star envelope. These cooling models were fit to superburst light curves to derive the depth and

energy-content of the burning layer (Cumming et al. 2006). Although they are a good match to the tail of superbursts, these models failed to reproduce the rise of the observed light curves. In particular, the cooling model light curves predict that the luminosity decreases between 100 to 1000 seconds after onset of the superburst, whereas the observed light curves are increasing in luminosity at that time. With the same assumption of complete burning, Weinberg & Bildsten (2007) also found declining light curves at 100–1000 seconds. In contrast, Keek & Heger (2011) carried out fully self-consistent simulations of superbursts that followed the carbon burning and energy deposition in detail. They instead found a rising luminosity during this phase of the superburst in some models (where the precursor did not dominate the rise).

This earlier work indicates that the phase of the superburst light curve prior to the peak at  $\sim 1000$  seconds is sensitive to the details of how the carbon combustion deposits energy in the neutron star envelope. The physics of how the

\* E-mail: l.keek@gatech.edu

carbon burning propagates is complex and may not be accurately captured by current 1D models. Rather than explicitly treating the hydrodynamic process of flame spreading, these models resolve the burning layers in the radial direction and include a 1D approximation to turbulence. In this paper we derive a useful constraint on such modelling by using the observed light curve to constrain the radial temperature profile left behind by carbon burning. This may inform other applications of carbon flames, such as the study of detonation and deflagration in Type Ia supernovae (e.g., [Woosley et al. 2011](#)).

Most of the current 24 (candidate) superbursts (e.g., [Keek et al. 2012](#); see [Negoro et al. 2012](#) and [Serino et al. 2014](#) for recent detections) are detected with instruments that have limited sensitivity (e.g., in 't Zand et al. 2003; [Keek et al. 2008](#)). Furthermore, the rise is often not observed due to gaps in the data from Earth occultation or passage through the South-Atlantic Anomaly (e.g., in 't Zand et al. 2004). The two highest quality observations were performed with the Proportional Counter Array (PCA; [Jahoda et al. 2006](#)) on-board the *Rossi X-ray Timing Explorer* (*RXTE*; [Bradt et al. 1993](#)). The first was a bright superburst from 4U 1820–30 ([Strohmayer & Brown 2002](#); [Ballantyne & Strohmayer 2004](#)). Its luminosity quickly reached the Eddington limit, which impedes the study of the intrinsic rise (e.g., in 't Zand & Weinberg 2010). The second PCA superburst observation was from 4U 1636–536 ([Strohmayer & Markwardt 2002](#); [Kuulkers et al. 2004](#)). It was not Eddington-limited, and at present it provides the only detailed observation of a superburst rise. Moreover, it is the only (super)burst for which spectral analyses were able to separate the direct burst emission from an evolving persistent component as well as photoionized reflection off the accretion disc ([Keek et al. 2014a,b](#)). Reflection refers to scattering of burst emission off the disc, which introduces features in the spectrum, such as a strong Fe  $K\alpha$  emission line, that depend on the ionization state of the disc ([Ballantyne 2004](#)).

In this paper we fit improved cooling models to the superburst light curve of 4U 1636–536. First we investigate the robustness of the light curve derived from the observations, in particular with respect to the influence of deviations of the neutron star's spectrum from a blackbody (Section 2). Subsequently, we create improved cooling models to constrain properties of the superbursting layer, including the slope of its temperature profile (Section 3). Comparison of the superburst tail to the best-fitting model light curve reveals interesting, but not entirely understood, behaviour (Section 4). Finally, we discuss how carbon combustion produces the inferred temperature gradient (Section 5).

## 2 RECONSTRUCTING THE OBSERVED LIGHT CURVE

For comparison to superburst cooling models, we set out to determine the most reliable light curve of neutron-star emission by separating out emission from and reflection off the accretion disc. In previous analyses, a blackbody was used to model the thermal spectrum of the neutron star ([Kuulkers et al. 2004](#); [Keek et al. 2014a,b](#)). A neutron star atmosphere spectrum is, however, expected to exhibit de-

viations from a blackbody due to, e.g., electron scattering which influence the blackbody parameters obtained in a spectral analysis ([Suleimanov et al. 2011](#)). To investigate how this affects the inferred net superburst light curve, we repeat the analysis procedure of [Keek et al. \(2014b\)](#) with neutron star atmosphere spectra instead of a blackbody.

### 2.1 Observations and spectral models

We reuse the PCA source spectra, instrumental background spectra, and response matrices that were created for [Keek et al. \(2014b\)](#) (see also [Keek et al. 2014a](#)). The spectra are collected in 64 s time intervals, and we consider the 3–20 keV energy range in our analysis. The superburst spans 4 *RXTE* orbits. As the signal is weaker in the final orbits, we use a single spectrum covering orbit 3. Orbit 4 is omitted, because the reflection features cannot be detected, and, therefore, the reflection signal cannot be separated from direct burst emission ([Keek et al. 2014b](#)). Spectral fitting is performed with XSPEC version 12.8.1 ([Arnaud 1996](#)), and  $1\sigma$  errors in the fit parameters are derived using a change in goodness of fit of  $\Delta\chi^2 = 1$ .

The spectra are described using 3 components: persistent emission from the accretion disc, direct thermal emission from the neutron star, and reflection of the thermal emission off the disc. The persistent part is modelled by a power law with an exponential high-energy cut-off at energy  $E_{\text{cutoff}}$ . For the other two components [Keek et al. \(2014b\)](#) employed a blackbody with temperature  $kT$  and a model of a reflected blackbody ([Ballantyne 2004](#)) at the same temperature, as a function of the disc's ionization parameter  $\xi$  (in units of  $\text{erg s}^{-1} \text{cm}$  in this paper). We refer to this model as **BB**. The spectral model further includes the photoelectric absorption model **vphabs** with an equivalent hydrogen column  $N_{\text{H}}$  (c.f., [Pandel et al. 2008](#)) and smoothing of the reflection component due to Doppler broadening and relativistic effects using the **rdblur** model ([Fabian et al. 1989](#)).

As an alternative for the blackbody, we use neutron star atmosphere spectra based on the models by [Suleimanov et al. \(2012\)](#) with a surface gravity of  $\log g = 14.3$  ( $g$  in units of  $\text{cm s}^{-2}$ ). Instead of the blackbody temperature, these models are a function of the ratio of the luminosity to the Eddington limited luminosity:  $L/L_{\text{Edd}}$ . We create two grids of atmosphere spectra each containing 100 values of the Eddington ratio, equidistant on a logarithmic scale, in the range  $10^{-3} \leq L/L_{\text{Edd}} \leq 1.08$ . These grids are optimized for the analysis of the superburst, as they have improved resolution at lower values of  $L/L_{\text{Edd}}$  compared to [Suleimanov et al. \(2011\)](#). One grid is for solar composition (model **S1**), and the other has a 100 times lower metal content (model **S001**). During the spectral fits with each grid, we fit for  $L/L_{\text{Edd}}$  and the normalization. For both grids we calculate photoionized reflection spectra using the code of [Ballantyne et al. \(2002\)](#) using the same procedure as [Ballantyne \(2004\)](#).

### 2.2 Spectral analysis

Because of the limited data quality, [Keek et al. \(2014b\)](#) found that certain parameters need to be constrained during the spectral fits. In particular, in the first *RXTE* orbit

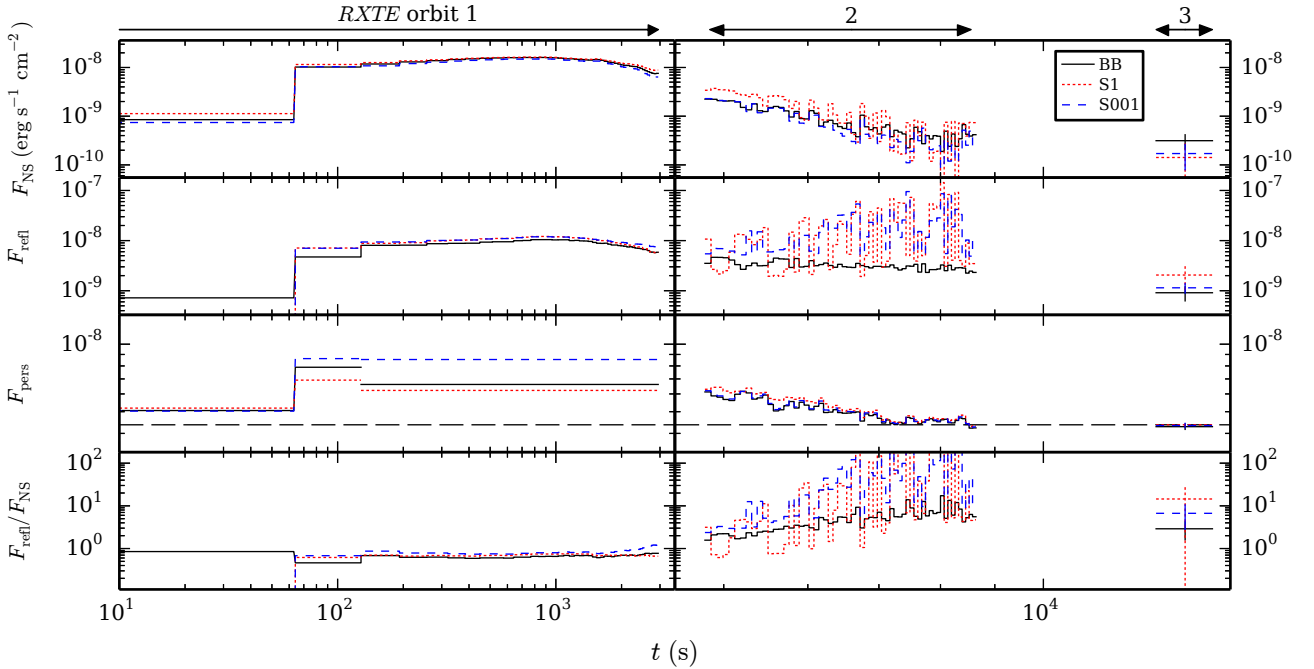


**Figure 1.** For 3 spectral models, flux as a function of time,  $t$ , for the direct neutron star emission ( $F_{\text{NS}}$ ), reflection ( $F_{\text{refl}}$ ), and persistent flux ( $F_{\text{pers}}$ ; the long-dashed line is the pre-superburst value). At the bottom we show the reflection fraction  $F_{\text{refl}}/F_{\text{NS}}$ .  $F_{\text{NS}}$  is modelled with a blackbody in **BB** and by a neutron star atmosphere in **S1** and **S001**. S1 assumes solar metallicity, whereas S001 uses a 100 times lower metallicity. The left and right panels each have a different horizontal scale. The  $1\sigma$  uncertainty is only indicated for the last data point. Excellent fits are obtained around the peak (left panel), where  $F_{\text{NS}}$  for the 3 models agrees at all times within 17%. Issues in the tail appear as large *unphysical* variations of  $F_{\text{refl}}$  for S1 and S001 (right panel; see also Section 5.4).

(excluding the first 128 s, which contain the pre-superburst flux and the precursor burst; see Figure 1) all spectra are fit simultaneously, and the normalizations of the power law and the direct neutron star component as well as  $N_{\text{H}}$  are tied between the spectra. The power-law index and  $E_{\text{cutoff}}$  are fixed to the pre-superburst values (Keek et al. 2014a). In orbits 2 and 3,  $E_{\text{cutoff}}$  is free, but the normalization of the neutron star component is fixed to the value obtained for the first orbit. This procedure yielded a good fit with model BB (Keek et al. 2014b), and repeating it with model S1 gives a similar goodness of fit. It does not, however, result in a good fit for S001 in the first orbit. To obtain a good fit with S001, we allow  $E_{\text{cutoff}}$  to vary in the first orbit, keeping its value tied between the spectra in the first orbit. The best-fitting value,  $E_{\text{cutoff}} = 6.17 \pm 0.07$ , is significantly larger than the pre-superburst value of  $E_{\text{cutoff}} = 4.80 \pm 0.06$  (Keek et al. 2014a). The  $\chi^2_{\nu}$  values obtained with S1 and S001 have a similar distribution as the values for model BB (Keek et al. 2014b).

S1 and S001 yield parameter values that are over-all quantitatively consistent with model BB. In particular, the weighted mean of  $\log \xi$  in the first orbit is within 2.8% of the BB value of  $\log \xi = 3.384 \pm 0.009$ , and in the second orbit all models exhibit a transition to a lower value of  $\log \xi$ . Furthermore, the Eddington ratio of the atmosphere models corresponds to an effective temperature of the neutron star photosphere that is lower than the measured blackbody temperature (Suleimanov et al. 2011). The ratio of the two is referred to as the colour correction factor,  $f_c$ . For model S1, we find  $f_c = 1.464 \pm 0.007$  when the Eddington ratio

peaks at  $L/L_{\text{Edd}} = 0.499 \pm 0.007$ , and it drops to a mean value of  $f_c = 1.295 \pm 0.010$  in the first 512 s of the second orbit where  $L/L_{\text{Edd}} = 0.101 \pm 0.002$ . Similarly, for model S001 the Eddington ratio peaks at  $L/L_{\text{Edd}} = 0.441 \pm 0.006$  with  $f_c = 1.511 \pm 0.008$ , and maintains a comparable value of  $f_c = 1.483 \pm 0.011$  while the Eddington ratio decreases to  $L/L_{\text{Edd}} = 0.0604 \pm 0.0013$  at the start of the second orbit. In both cases the behaviour is consistent with the theoretical predictions for the considered values of  $L/L_{\text{Edd}}$ :  $f_c$  is close to constant for a metal-poor atmosphere, but it exhibits larger variations for solar composition (Suleimanov et al. 2011, 2012). The deviations of the spectrum from a blackbody are, therefore, too small for the data to discriminate between S1 and S001, and the models simply behave as predicted.

The neutron star fluxes,  $F_{\text{NS}}$ , are consistent for BB, S1, and S001: in the first orbit within 17% (Figure 1). Because S001 has a higher  $E_{\text{cutoff}}$ , its persistent flux,  $F_{\text{pers}}$ , is larger by 29% in the first orbit. In the following orbits S001's  $F_{\text{pers}}$  is consistent with BB and S1. Furthermore, in the second orbit the reflected neutron star flux,  $F_{\text{refl}}$ , of both S1 and S001 exhibits strong variations. For some spectra the fit prefers low values of  $L/L_{\text{Edd}}$ , which require large bolometric corrections and produce unrealistically large values for  $F_{\text{refl}}$  and for the reflection fraction  $F_{\text{refl}}/F_{\text{NS}}$ . For other spectra, the fits find more reasonable values of  $F_{\text{refl}}$ , and this ‘track’ is closer to the fluxes and reflection fractions obtained for BB (Figure 1). We attribute these issues to the increasingly poor data quality in the superburst tail.

Because of the similarity of  $F_{\text{NS}}$  for all models around the peak, and the issues of S1 and S001 in the tail, we choose

model BB for comparison with theoretical light curves. We calculate the net superburst luminosity from  $F_{\text{NS}}$  assuming isotropic emission by the neutron star at a distance of  $6.0 \pm 0.5$  kpc (Galloway et al. 2008). We do not include the distance error in the uncertainty of the luminosity data points, but it is included as a systematic uncertainty when we fit cooling models (Section 3). Because of the mentioned issues in the tail of the superburst, we first focus on the rise and the peak of the superburst in the first orbit. In Section 4 we look at the tail in more detail.

### 3 COOLING MODELS FOR THE SUPERBURST LIGHT CURVE

In this section, we make models of the superburst light curve by assuming that the nuclear burning occurs rapidly after ignition, leaving behind a temperature profile that we then take as an initial condition for the subsequent cooling. We show that the light curve slope during the rising phase at 100–100 s constrains the temperature profile in the layer set by carbon burning.

#### 3.1 Details of the models

To calculate the cooling of the heated layer, we follow the approach of Cumming & Macbeth (2004) and Cumming et al. (2006). The main differences from those calculations are in the choice of initial temperature profile for the cooling, a correction to the radiative opacities used in those papers, and a more accurate outer boundary condition.

To follow the cooling of the layer, we integrate<sup>1</sup> the heat equation

$$c_P \frac{\partial T}{\partial t} = \frac{\partial F}{\partial y} - \epsilon_\nu; \quad F = \frac{4acT^3}{3\kappa} \frac{\partial T}{\partial y}, \quad (1)$$

where  $F$  is the heat flux,  $\epsilon_\nu$  the neutrino emissivity,  $T$  the temperature,  $y$  the column depth,  $\kappa$  the opacity,  $a$  the radiation constant, and  $c$  the speed of light. We use the method of lines, in which we difference the spatial part of these equations on a grid in column depth with a constant spacing  $\Delta x = \Delta \ln y$ , and then integrate the stiff set of ordinary differential equations that result forward in time using an implicit integrator. The inner zone is set to be a factor of 1000 deeper in column than the ignition depth. We typically set the outer zone in our time-dependent calculation at a column depth  $y_t = 10^8$  g cm<sup>-2</sup>, which is a small fraction of the typical fuel column ( $\lesssim 10^{-3}$ ). We adopt as default neutron star parameters  $M = 1.4 M_\odot$  and  $R = 12$  km giving a gravity  $g_{14} = g/10^{14}$  cm s<sup>-2</sup> = 1.60 and redshift  $1 + z = (1 - 2GM/c^2R)^{-1/2} = 1.24$ , where  $g = (GM/R^2)(1+z)$ . This choice of  $g$  is slightly smaller than what was used for the atmosphere spectra (Section 2.1), but there is no problem with consistency, because we will fit the cooling models to the light curve from spectral model BB. The calculation is Newtonian in that redshift variations across the thin layer are ignored. Instead, we set the gravity to be a constant and then redshift the time and flux to infinity to compare to observations.

<sup>1</sup> The code used in this paper is available at <https://github.com/andrewcumming/burstcool>.

The microphysics input is as follows. For the equation of state of the electrons, we use the fits of Paczynski (1983), except for the electron heat capacity which is a modified version of the Paczynski (1983) formula that has the correct limits for non-degenerate and degenerate electrons (Schatz et al. 2003). The electron Fermi energy is calculated as needed according to Chabrier & Potekhin (1998). Coulomb corrections for the ions are calculated using the results of Potekhin & Chabrier (2000) (see their Equation. 17). The free-free and electron scattering radiative opacities are calculated following Schatz et al. (1999). When forming the total opacity, we include an additional factor from Potekhin & Yakovlev (2001) to account for the fact that Rosseland mean opacities are not additive (see discussion in Stevens et al. 2014). The thermal conductivity is calculated by implementing the fitting formulas of Potekhin et al. (1999). Neutrino emissivities due to the plasma, pair, and bremsstrahlung processes are included using the fitting formulae from Schinder et al. (1987) and Haensel et al. (1996).

The boundary condition  $F(T)$  at  $y = y_t$  is determined from a grid of constant flux atmospheres which are integrated separately. The key region is the “sensitivity strip” at column depths  $\sim 10^7$ – $10^8$  g cm<sup>-2</sup>, which is assumed to consist of <sup>56</sup>Ni in our default model (matching the composition of the cooling layer). The layers  $y < 10^7$  g cm<sup>-2</sup> are pure helium (the composition at low density does not affect the  $F$ – $T$  relation, being out of the sensitivity strip).

#### 3.2 The initial temperature profile

The starting temperature profile for the cooling is set to be a power law with depth,  $T_f(y) = T_b(y/y_b)^\alpha$ . The normalization  $T_b$  is chosen such that the average energy input is a specified value  $E_{\text{nuc}} = E_{18} 10^{18}$  erg g<sup>-1</sup>,

$$\int_{y_t}^{y_b} dy \int_{T_i}^{T_f(y)} c_P dT = y E_{\text{nuc}}. \quad (2)$$

Since  $T_f \gg T_i$ , the light curves are not very sensitive to the choice of  $T_i$ ; for simplicity we set  $T_i = 2 \times 10^8$  K, constant with depth.

The effect of the choice of the slope of the temperature profile  $\alpha$  on the light curve is shown in Figure 2. The light curves shown have the same total energy release and depth, but different choices of  $\alpha$ . We also show two other choices of initial temperature profile. One is to assume no heat transport, and burn the fuel locally and instantaneously. This was the assumption of Cumming & Macbeth (2004) and gives a profile with  $\alpha \approx 1/8$ . The second is an adiabatic initial profile, with  $d \ln T / d \ln P = \nabla_{\text{ad}}$  at each depth. This could result if convection is able to efficiently mix the burning layer.

Figure 2 shows that different choices of  $\alpha$  result in different light curve slopes at times 100–1000 s before the light curve peak. Smaller values of  $\alpha \lesssim 0.21$  lead to a luminosity that falls with time during this phase; larger values of  $\alpha$  give a luminosity that increases with time. We see that a measurement of the slope of the cooling curve at early times is a direct measure of the slope of the temperature profile in the layer immediately following burning. This is explicitly shown in Figure 3 which shows the temperature slope  $\alpha$  as a function of the slope of the light curve measured at 200 seconds.

The form of the relation between  $\alpha$  and  $d \ln L / d \ln t$

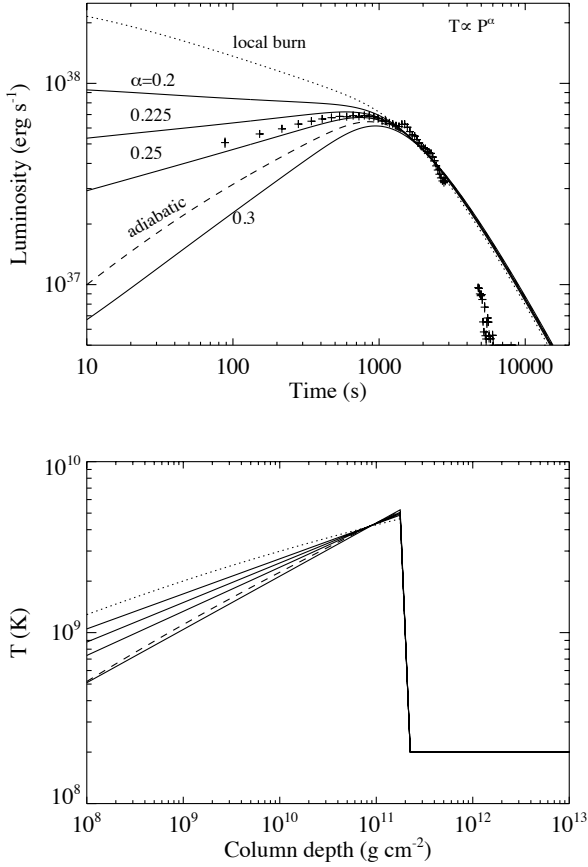


**Figure 2.** Model light curves (top panel) with the same total energy release and ignition depth, but different initial temperature profiles (bottom panel). The solid curves have  $T \propto P^\alpha$  with (top to bottom)  $\alpha = 0.2, 0.225, 0.25$  and  $0.3$ . The dot-dashed curve assumes local deposition of energy ( $\alpha \approx 1/8$  as in Cumming & Macbeth 2004); the dashed curve has an adiabatic profile  $d \ln T / d \ln P = \nabla_{\text{ad}}$ . For all models the ignition column is  $2 \times 10^{11} \text{ g cm}^{-2}$  and energy release  $E_{18} = 0.25$ . Crosses are the data points of the observation of 4U 1636–536, where time starts at the onset of the precursor ( $t = 72 \text{ s}$  in Figure 1).

shown in Figure 3 can be understood using the analytic estimates for the early time light curve from Appendix A of Cumming et al. (2006). Assuming constant opacity for simplicity, they modelled the early time light curve by writing the flux  $F \propto T^4/y$ , where  $y$  is the depth that the cooling wave has reached at a time  $t$ . This depth is given by setting the thermal time-scale to the current time  $t = t_{\text{therm}} \propto y^{7/4}/T^2$ . With a temperature profile of the form  $T \propto y^\alpha$ , we find  $d \ln L / d \ln t = -4(4\alpha - 1)/(8\alpha - 7)$ . This qualitatively agrees with Figure 3, but is not accurate in detail as we might expect from a simple constant opacity estimate. We find that  $d \ln L / d \ln t = 5(\alpha - 0.21)$  is a good approximation to the numerical results, shown in Figure 3 as a dotted line.

### 3.3 Comparison to the data

The data for the 4U 1636–536 light curve is plotted in Figure 2. We take the start time  $t = 0$  at the onset of the precursor burst (e.g., Keek et al. 2014a), which corresponds

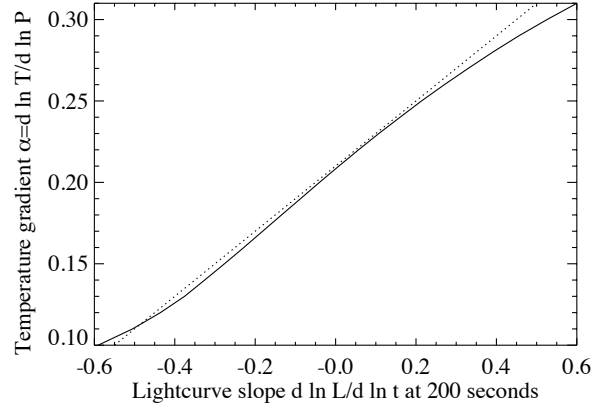


**Figure 3.** The slope of the light curve at 200 seconds ( $d \ln L / d \ln t$ ) as a function of the temperature slope in the layer at the onset of cooling  $T \propto P^\alpha$ . The dotted line is the analytically-motivated fit  $d \ln L / d \ln t = 5(\alpha - 0.21)$ .

to  $t = 72 \text{ s}$  in Figure 1. As described by Cumming et al. (2006), the total energy release is constrained by the luminosity of the early part of the light curve (before the peak at  $\approx 10^3$  seconds), whereas the depth of the layer is constrained by the cooling time-scale associated with the tail of the burst (after  $10^3$  seconds). We find that an energy release  $E_{18} \approx 0.25$  and a depth  $y \approx 2 \times 10^{11} \text{ g cm}^{-2}$  give a good fit to the data. In addition, as can be seen in Figure 2, the data strongly constrain the temperature profile to have  $\alpha = 0.25$ . The observed slope  $d \ln L / d \ln t$  is positive, ruling out the local burning temperature profile, but also not steep enough to match the adiabatic profile.

The curves shown in Figure 2 are for a particular choice of neutron star mass and radius, composition of the burning products, and distance (Section 3.1). We investigate the robustness of our conclusions to these parameters. We use the `emcee` Markov Chain Monte Carlo (MCMC) code (Foreman-Mackey et al. 2013) to explore the parameter space. In doing so, we fit the data for  $t < 1400 \text{ s}$  only. This includes the peak of the light curve, but excludes most of the decay. As can be seen in Figure 2, the observed luminosity shows abrupt changes of slope during the decay phase which can bias the fits, since there are many data points in the decay part of the light curve. By including the data in the rise and peak only we are able to obtain good fits to the data ( $\chi_\nu^2 \approx 1$ ) and we still obtain a tight constraint on the allowed column depth.

We find that the derived values of  $E_{18}$ ,  $y$  and especially  $\alpha$  are not very sensitive to the uncertainties in the other parameters. For a fixed distance, we find that changing the heavy element composition, for example from Fe to Si, or the mass and radius of the neutron star within typical values, e.g.  $1.2$  to  $2.0 M_\odot$  and  $10$ – $13 \text{ km}$  changes the derived energy and column depth by  $\approx 10\%$ , with much smaller changes in  $\alpha$ . Changing the distance has a larger effect on the derived energy and column depth (Cumming et al. 2006). For example, with a prior on distance from  $4$  to  $8 \text{ kpc}$ , we find a range of  $E_{18} \approx 0.24$ – $0.32$  and  $y \approx 1.5$ – $4 \times 10^{11} \text{ g cm}^{-2}$ . The distribution of allowed slopes is still rather narrow, with  $\alpha = 0.242 \pm 0.004$ .

#### 4 THE TAIL OF THE SUPERBURST

Although the cooling models are in excellent agreement with the rise and peak of the observed light curve, in the tail  $F_{\text{NS}}$  decreases much faster than predicted (see the corresponding luminosity in Figure 2). As the normalization of the neutron star spectral component is kept fixed in the tail, the behaviour of the flux is purely due to the temperature evolution. This implies exceptionally fast cooling of the neutron star atmosphere.

As an alternative assumption for the normalization of the BB blackbody component in the tail, we fix the reflection fraction to the mean value in the first orbit:  $F_{\text{refl}}/F_{\text{NS}} = 0.665 \pm 0.012$  (model **BB<sub>frac</sub>**). The physical implication of a constant reflection fraction is that the accretion geometry is unchanged during the superburst. The goodness of fit for **BB<sub>frac</sub>** is similar as the other models. This produces a slower decay that closely follows the trend of the cooling model (Figure 4). To quantify how well **BB<sub>frac</sub>** matches the cooling model, we take the ratio of  $F_{\text{NS}}$  to the model flux. In orbit 2, the weighted mean is  $0.858 \pm 0.009$ . This implies that the actual reflection fraction in the tail is  $0.43 \pm 0.02$ . A decrease of the reflection fraction may be expected if the disc was puffed up by X-ray heating in the peak, and returned to a flatter geometry as the illumination was reduced in the tail (e.g., [Ballantyne & Everett 2005](#); [Lapidus & Sunyaev 1985](#)).

Model **BB<sub>frac</sub>** has a similarly fast decrease of the blackbody temperature as **BB**. The slower decline of the flux, therefore, implies that the temperature decrease is partially compensated by an increase in the normalization. In the final 1024 s of the second orbit, the weighted mean of the ratio of  $F_{\text{NS}}$  for **BB<sub>frac</sub>** and **BB** is  $5.2 \pm 0.2$ . As the blackbody normalization is proportional to the apparent emitting area, this corresponds to a radius increase with respect to the peak by a factor  $2.27 \pm 0.04$ . The appearance of radius expansion in this part of the superburst is puzzling, and in Section 5.4 we further discuss the challenges of the interpretation of the superburst tail.

#### 5 DISCUSSION

We first discuss the main result from our analysis: constraints on the superburst parameters from cooling models, including the temperature profile created by the carbon flame. Next we compare the inferred ignition column to the observational constraints on the accreted column. Finally, we discuss the robustness of the observed light curve and in particular the issues with the interpretation of the spectra in the superburst tail.

##### 5.1 Retracing the carbon flame with cooling models

Carbon combustion has been studied extensively in the context of Type Ia supernovae, in particular to investigate whether carbon flames propagate as a detonation and/or a deflagration (e.g., [Woosley et al. 2011](#)). Superbursts provide a unique opportunity to study carbon flames, as they occur close to the surface of the star, without the thermonuclear event disrupting it. [Weinberg & Bildsten \(2007\)](#) calculated the propagation of a detonation through the carbon layer. At

depths  $y \lesssim y_{\text{det}} \approx 2 \times 10^{11} \text{ g cm}^{-2}$  the time-scale to burn carbon is longer than a dynamical time-scale, so that the detonation ceases and the shock runs ahead of the burning. The column depth that we infer for the 2001 4U 1636–536 superburst is about this depth, suggesting that a detonation did not likely occur in this superburst.

Our fits with cooling models find a temperature profile with power-law slope  $\alpha \simeq 1/4$ , whereas complete local burning produces  $\alpha = 1/8$ . One way in which a temperature profile with  $\alpha > 1/8$  could come about is if the burning becomes more and more incomplete at low densities. [Weinberg & Bildsten \(2007\)](#) pointed out that the shallow superburst light curves imply a steeper temperature gradient than would result from a complete burn. They suggested that perhaps the convective deflagration leaves behind an increasing amount of unburned fuel as it moves to lower densities. Since local instantaneous burning produces a temperature  $T_f \propto E_{18}^{1/2} y^{1/8}$  ([Cumming & Macbeth 2004](#)),  $T_f \propto P^\alpha$  implies  $E_{18} \propto P^{(8\alpha-1)/4}$ . For  $\alpha = 1/4$  this is  $E_{18} \propto P^{1/4}$ . If the fuel layer initially has a homogeneous composition, this describes the fraction of the fuel that is burned as a function of depth. For example, assuming that at the ignition depth 100% was burned, we estimate that only 50% was burned at an order of magnitude shallower depth. Integrating over all depths, as much as 20% by mass of the fuel may be left unburned.

Sound waves or a shock generated by carbon ignition have been suggested to heat the atmosphere above the superburst fuel layer and induce hydrogen and helium burning, which would power the precursor bursts observed at the onset of superbursts ([Weinberg & Bildsten 2007](#); [Keek & Heger 2011](#); [Keek 2012](#)). The tail of these precursors and subsequent stable burning of freshly accreted hydrogen and helium may lower the steepness of the light curve ([Keek et al. 2012](#)). We have reduced this effect by starting our fits well after the precursor.

[Keek & Heger \(2011\)](#) and [Keek et al. \(2012\)](#) calculated fully self-consistent 1d multi-zone models of superbursts. The light curves show both rising and declining phases at times hundreds to thousands of seconds, depending on the accretion rates and base fluxes chosen for the models. For example, the superburst light curve shown in Figure 3 of [Keek et al. \(2012\)](#) shows a rise between  $\approx 30$  and 300 seconds, and then a declining light curve from 300 to  $10^4$  seconds. Our new cooling models are able to reproduce the light curves of these models. In a future publication, we will study in detail how the measured temperature profile is reproduced in these 1d models.

Given that carbon burning to nickel produces  $1.0 \text{ MeV u}^{-1} = 0.96 \times 10^{18} \text{ erg g}^{-1}$  ([Schatz et al. 2003](#), ignoring a possible contribution from photodisintegration), the measured  $E_{18}$  translates to a carbon mass fraction of 26%. This is consistent with the value previously measured with local burn models ([Cumming et al. 2006](#)). Furthermore, we find an ignition column that is less than half as large as previously measured. This is due to the different shape of our new model light curves. Therefore, the inferred column depths for other superburst observations may have been too large as well ([Cumming et al. 2006](#); [Keek et al. 2008](#); [Kuulkers et al. 2010](#); [Altamirano et al. 2012](#)). For fits to the light curve of the candidate superburst from EXO 1745–248, [Altamirano et al. \(2012\)](#) used an early version of our

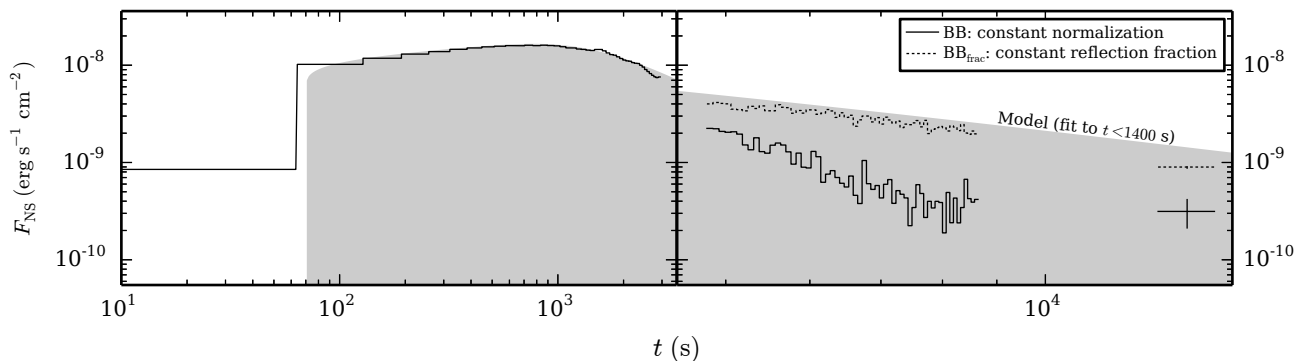


**Figure 4.** Comparison of two derived superburst light curves to the cooling model that fits best to the first 1400 s (top of the shaded region; see Section 3). **BB** assumes a constant normalization of the spectral component that describes the thermal emission of the neutron star, whereas spectral model **BB<sub>frac</sub>** assumes the reflection fraction to be constant. The left and right panels and their scale are the same as in Figure 1.

cooling models with an  $\alpha$  value close to the one that we obtain, in anticipation of this paper. Because the onset of that superburst was not observed, it did not itself provide a constraint on  $\alpha$ . The 2001 superburst from 4U 1636–536 is the highest quality observation of the rise and peak, and improved measurements of superburst parameters including  $\alpha$ , therefore, require new superburst observations with future large-area X-ray telescopes such as NASA’s *Neutron Star Interior Composition Explorer* (*NICER*, scheduled for launch in 2016; [Gendreau et al. 2012](#)).

## 5.2 Accretion history

Three other superbursts have been observed from 4U 1636–536. The one immediately preceding the superburst discussed in this paper was 1.75 yr earlier ([Kuulkers 2009](#); no superburst has been observed from this source afterwards). From the Multi Instrument Burst ARchive (MINBAR; [Keek et al. 2010](#)), which is the largest catalogue of X-ray observations of bursting sources, we select all 132 *RXTE* PCA ([Galloway et al. 2008](#)) and *BeppoSAX* WFC ([Cornelisse et al. 2003](#)) observations in that time interval. The observations are spread out in time, and constitute a total exposure time of 1.44 Ms. The unabsorbed persistent 3 – 25 keV flux varies between observations by a factor 2.8. We determine its time-averaged value as the mean of all flux measurements weighted by the duration of each observation:  $F_{\text{pers}} = (4.17 \pm 0.07) \times 10^{-9} \text{ erg s}^{-1} \text{ cm}^{-2}$ . Employing a bolometric correction of 1.1 ([Fiocchi et al. 2006](#)) and a distance of 6.0 kpc, the average persistent luminosity is  $L_{\text{pers}} = (1.98 \pm 0.03) \times 10^{37} \text{ erg s}^{-1}$  (distance uncertainty not included). For 1.75 years of accretion on to a neutron star with parameters as described in Section 3.1, this corresponds to an accretion column of  $y_{\text{acc}} = (3.53 \pm 0.05) \times 10^{11} \text{ g cm}^{-2}$ , assuming the efficiency of releasing gravitational potential energy in X-rays is 100%. Because of our assumptions, the actual uncertainty is probably at least several tens of percent. Given the best-fitting value for  $y_{\text{ign}}$  from cooling models (Section 3.3),  $y_{\text{acc}}$  can accommodate 2 superbursts:  $y_{\text{acc}}/y_{\text{ign}} = 1.8 \pm 0.2$ , where we use the MCMC-derived error on  $y_{\text{ign}}$  without the uncertainty in the distance, which drops out. We regard it likely that an extra superburst occurred

roughly in the middle of the preceding 1.75 years. Around this time no superburst has been detected with, e.g., the All-Sky Monitor on *RXTE* (e.g., [Kuulkers 2009](#)) or other instruments, but this could easily be attributed to the sparse coverage of the source by the X-ray observatories that were operational at the time.

## 5.3 Robustness of the observed rise and peak

In the rise and around the peak of the superburst light curve, the spectrum clearly separates in three components, one of which we interpret as the direct thermal emission from the neutron star. The best-fitting parameters of the considered spectral models for this component can be somewhat different: e.g., the peak value of  $L/L_{\text{Edd}}$  for the metal-poor atmosphere model is 12% lower than for the solar-composition atmosphere. Nevertheless, the neutron star flux is consistent between the spectral models of both a blackbody and neutron star atmospheres. All models result in a similar goodness of fit.

After the peak, at  $t \simeq 1400 \text{ s}$  the light curve exhibits some variability on time-scales of  $\sim 10^2 \text{ s}$ . Compared to the cooling model fit to the data at earlier times, the flux variations are both above and below the model, and may have a similar origin as the so-called “achromatic” variability, which is typically observed in some Eddington-limited bursts including the 1999 superburst from 4U 1820–30 ([in ’t Zand et al. 2011](#)). In our spectral fits, the variability is strongest in the neutron star component. Since we constrained the persistent component to be the same throughout the first orbit (Section 2.2), however, it is possible that the variability is actually part of the persistent emission. Instead of the neutron star envelope, it may be more likely that the physical origin of the variability is found in, e.g., instabilities in the accretion disc.

A systematic uncertainty in the conversion of flux to luminosity is introduced by anisotropy of the emission. Assuming an inclination angle of  $60^\circ$  (e.g., [Pandel et al. 2008](#)) and a thin flat disc, the neutron star’s intrinsic luminosity is  $1/3$  larger than the value we obtained under the assumption of isotropic emission ([Fujimoto 1988](#)). Its main effect is an equivalent increase in  $E_{18}$ .

The most robust part of the superburst light curve is, therefore, the rise and peak, until the onset of variability. We, therefore, fit cooling models exclusively to this part.

#### 5.4 Interpretation of the spectra in the tail

In the tail, the observed signal is weaker, and it is challenging to separate and interpret the spectral components. Especially the spectral fits with atmosphere models are problematic, as at certain times the fits cannot distinguish between very low values of  $L/L_{\text{Edd}}$  and more reasonable values (Figure 1). Even when disregarding these unphysical solutions, for all spectral models the neutron star envelope’s temperature appears to drop faster than predicted by cooling models (Figure 2). Schatz et al. (2014) pointed out that an URCA neutrino cooling process could operate in the outer crust, depending on the mixture of nuclei present, and suggested that the cooling could affect the shape of superburst tails. However, the drop in temperature that we observe here is much faster than expected even with URCA cooling. The disagreement between the model and data occurs immediately after the peak, implying that the URCA cooling source would have to be at a very shallow depth close to the carbon ignition depth, which is unlikely. Furthermore, fully self-consistent 1d models of superbursts have similar problems in simultaneously fitting the rise and tail (Keek & Heger 2011, albeit this comparison was against a lightcurve that did not account for increased persistent emission nor reflection), indicating that the mismatch is not due to, e.g., late-time residual burning. The strong temperature drop is found for the different constraints on the normalization of the neutron star spectral component (BB and  $\text{BB}_{\text{frac}}$ ) as well as for the combined neutron star and reflection components (Keek et al. 2014a). If the neutron star’s emitting area is kept constant, this directly translates into a fast decline of  $F_{\text{NS}}$  (BB), whereas with a constant reflection fraction  $F_{\text{NS}}$  more closely matches the best-fitting cooling model ( $\text{BB}_{\text{frac}}$ ; Figure 4).

The slower decay of  $F_{\text{NS}}$  for  $\text{BB}_{\text{frac}}$  requires a radius increase of a factor  $2.27 \pm 0.04$  in the tail, even though radius expansion is typically expected to occur only at larger luminosities near the Eddington limit. Alternatively, deviations of the neutron star spectrum from a blackbody have manifested itself as increased normalizations in the tail of short X-ray bursts (e.g., Suleimanov et al. 2011). By fitting with atmosphere models (S1 and S001), we confirm that this plays no role in our case, because we fix the normalization in the tail. Furthermore, the neutron star spectral component is consistent with a single-temperature blackbody, indicating that the fast temperature decrease is intrinsic to the neutron star. In this case the radius increase must be intrinsic to the star as well, and not an anisotropy effect (Lapidus & Sunyaev 1985; Fujimoto 1988).

Finally, as the flux in the tail is dominated by the persistent component (Figure 1; see also Keek et al. 2014a,b), mischaracterisation of this component could influence the results of the analysis in this part of the superburst. For example, a boundary or spreading layer is thought to be present between the accretion disc and the neutron star atmosphere (Inogamov & Sunyaev 1999). The fraction of the neutron star covered by this layer may evolve during the superburst. It is, however, challenging to decompose even high-

quality spectra of persistent emission (Revnitsev et al. 2013). Better constraints on the persistent spectrum may be provided by a future superburst observation with energy coverage extending below 1 keV, for example with *XMM-Newton* (Jansen et al. 2001) or *NICER* (Gendreau et al. 2012).

## 6 CONCLUSIONS

The 2001 *RXTE*/PCA superburst from 4U 1636–536 is the only high-quality observation of the intrinsic rise and peak of a superburst. We separate the direct thermal emission from the neutron star from evolving reflection and persistent contributions to the spectrum, and evaluate the robustness of the derived light curve with respect to the choice of spectral model, including neutron star atmosphere models. In the tail of the burst, where the count rate is lowest, the interpretation of the spectrum is ambiguous. The rise and peak, however, provide a robust net superburst light curve. We show how the steepness of the rise is determined by the slope of the temperature profile in the neutron star envelope. The light curve is fit with new cooling models that take this feature into account. The temperature slope with pressure is constrained to be  $T \propto P^\alpha$  with  $\alpha \approx 0.25$ . This is inconsistent with complete burning of the carbon to iron group elements, and implies significant incomplete burning. Theoretical calculations of the propagation of carbon flames in neutron star envelopes are needed to explain the observed slope. Finally, the observational upper limit to the recurrence time of this superburst is 1.75 yr, but we find that in that time enough fuel was accumulated for two superbursts. This implies that the superburst directly prior to the one in 2001 had escaped detection.

## ACKNOWLEDGEMENTS

We are grateful for discussions with E. F. Brown, A. Heger, and D. K. Galloway. LK and DRB acknowledge support from NASA ADAP grant NNX13AI47G and NSF award AST 1008067. AC was supported by the National Sciences and Engineering Research Council (NSERC) of Canada. AC is an associate of the CIFAR Cosmology and Gravity program. VS was supported by German Research Foundation (DFG) grant WE 1312/48-1. This paper uses preliminary analysis results from the Multi-INstrument Burst ARchive (MINBAR), which is supported under the Australian Academy of Science’s Scientific Visits to Europe program, and the Australian Research Council’s Discovery Projects and Future Fellowship funding schemes. We made use of the emcee code by Foreman-Mackey et al., available at <http://dan.iel.fm/emcee>.

## References

- Altamirano D., et al., 2012, *MNRAS*, **426**, 927
- Arnaud K. A., 1996, in Jacoby G. H., Barnes J., eds, *Astronomical Society of the Pacific Conference Series Vol. 101, Astronomical Data Analysis Software and Systems V*. p. 17
- Ballantyne D. R., 2004, *MNRAS*, **351**, 57
- Ballantyne D. R., Everett J. E., 2005, *ApJ*, **626**, 364
- Ballantyne D. R., Strohmayer T. E., 2004, *ApJ*, **602**, L105



- Ballantyne D. R., Fabian A. C., Ross R. R., 2002, *MNRAS*, **329**, L67
- Bradt H. V., Rothschild R. E., Swank J. H., 1993, *A&AS*, **97**, 355
- Chabrier G., Potekhin A. Y., 1998, *Phys. Rev. E*, **58**, 4941
- Cornelisse R., Heise J., Kuulkers E., Verbunt F., in 't Zand J. J. M., 2000, *A&A*, **357**, L21
- Cornelisse R., et al., 2003, *A&A*, **405**, 1033
- Cumming A., Bildsten L., 2001, *ApJ*, **559**, L127
- Cumming A., Macbeth J., 2004, *ApJ*, **603**, L37
- Cumming A., Macbeth J., in 't Zand J. J. M., Page D., 2006, *ApJ*, **646**, 429
- Fabian A. C., Rees M. J., Stella L., White N. E., 1989, *MNRAS*, **238**, 729
- Fiocchi M., Bazzano A., Ubertini P., Jean P., 2006, *ApJ*, **651**, 416
- Foreman-Mackey D., Hogg D. W., Lang D., Goodman J., 2013, *PASP*, **125**, 306
- Fujimoto M. Y., 1988, *ApJ*, **324**, 995
- Galloway D. K., Muno M. P., Hartman J. M., Psaltis D., Chakrabarty D., 2008, *ApJS*, **179**, 360
- Gendreau K. C., Arzoumanian Z., Okajima T., 2012, in Society of Photo-Optical Instrumentation Engineers (SPIE) Conference Series. , doi:10.1117/12.926396
- Haensel P., Kaminker A. D., Yakovlev D. G., 1996, *A&A*, **314**, 328
- Inogamov N. A., Sunyaev R. A., 1999, *Astronomy Letters*, **25**, 269
- Jahoda K., Markwardt C. B., Radeva Y., Rots A. H., Stark M. J., Swank J. H., Strohmayer T. E., Zhang W., 2006, *ApJS*, **163**, 401
- Jansen F., et al., 2001, *A&A*, 365, L1
- Keek L., 2012, *ApJ*, **756**, 130
- Keek L., Heger A., 2011, *ApJ*, **743**, 189
- Keek L., in 't Zand J. J. M., Kuulkers E., Cumming A., Brown E. F., Suzuki M., 2008, *A&A*, **479**, 177
- Keek L., Galloway D. K., in 't Zand J. J. M., Heger A., 2010, *ApJ*, **718**, 292
- Keek L., Heger A., in 't Zand J. J. M., 2012, *ApJ*, **752**, 150
- Keek L., Ballantyne D. R., Kuulkers E., Strohmayer T. E., 2014a, *ApJ*, **789**, 121
- Keek L., Ballantyne D. R., Kuulkers E., Strohmayer T. E., 2014b, *ApJ*, **797**, L23
- Kuulkers E., 2009, *The Astronomer's Telegram*, **2140**, 1
- Kuulkers E., in 't Zand J., Homan J., van Straaten S., Altamirano D., van der Klis M., 2004, in Kaaret P., Lamb F. K., Swank J. H., eds, *American Institute of Physics Conference Series* Vol. 714, *X-ray Timing 2003: Rossi and Beyond*. pp 257–260 ([arXiv:astro-ph/0402076](https://arxiv.org/abs/astro-ph/0402076)), doi:10.1063/1.1781037
- Kuulkers E., et al., 2010, *A&A*, **514**, A65+
- Lapidus I. I., Sunyaev R. A., 1985, *MNRAS*, **217**, 291
- Lewin W. H. G., van Paradijs J., Taam R. E., 1993, *Space Science Reviews*, **62**, 223
- Negoro H., et al., 2012, *The Astronomer's Telegram*, **4622**, 1
- Paczynski B., 1983, *ApJ*, **264**, 282
- Pandel D., Kaaret P., Corbel S., 2008, *ApJ*, **688**, 1288
- Potekhin A. Y., Chabrier G., 2000, *Phys. Rev. E*, **62**, 8554
- Potekhin A. Y., Yakovlev D. G., 2001, *A&A*, **374**, 213
- Potekhin A. Y., Baiko D. A., Haensel P., Yakovlev D. G., 1999, *A&A*, **346**, 345
- Revnivtsev M. G., Suleimanov V. F., Poutanen J., 2013, *MNRAS*, **434**, 2355
- Schatz H., Bildsten L., Cumming A., Wiescher M., 1999, *ApJ*, **524**, 1014
- Schatz H., Bildsten L., Cumming A., 2003, *ApJ*, **583**, L87
- Schatz H., et al., 2014, *Nature*, **505**, 62
- Schinder P. J., Schramm D. N., Wiita P. J., Margolis S. H., Tubbs D. L., 1987, *ApJ*, **313**, 531
- Serino M., et al., 2014, *The Astronomer's Telegram*, **6668**, 1
- Stevens J., Brown E. F., Cumming A., Cyburt R., Schatz H., 2014, *ApJ*, **791**, 106
- Strohmayer T. E., Brown E. F., 2002, *ApJ*, **566**, 1045
- Strohmayer T. E., Markwardt C. B., 2002, *ApJ*, **577**, 337
- Suleimanov V., Poutanen J., Werner K., 2011, *A&A*, **527**, A139+
- Suleimanov V., Poutanen J., Werner K., 2012, *A&A*, **545**, A120
- Weinberg N. N., Bildsten L., 2007, *ApJ*, **670**, 1291
- Woosley S. E., Kerstein A. R., Aspden A. J., 2011, *ApJ*, **734**, 37
- in 't Zand J. J. M., Weinberg N. N., 2010, *A&A*, **520**, A81
- in 't Zand J. J. M., Kuulkers E., Verbunt F., Heise J., Cornelisse R., 2003, *A&A*, **411**, L487
- in 't Zand J. J. M., Cornelisse R., Cumming A., 2004, *A&A*, **426**, 257
- in 't Zand J. J. M., Galloway D. K., Ballantyne D. R., 2011, *A&A*, **525**, A111

This paper has been typeset from a  $\text{\TeX}/\text{\LaTeX}$  file prepared by the author.